nature communications



Article

https://doi.org/10.1038/s41467-025-60340-0

A self-sufficient system for fog-to-water conversion and nitrogen fertilizer production to enhance crop growth

Received: 28 March 2025

Accepted: 19 May 2025

Published online: 27 May 2025

Check for updates

Zhenwen Zhang^{1,4}, Tong Li ^{1,4}, Yongjiu Yuan^{1,4}, Zhi Zhang^{1,4}, Chen Ling¹, Xiaoxue Yao¹, Hongbo Wang ¹, Wai Kin Lo ¹, Qili Xu^{1,2}, Jun Liu ¹, Yun Hau Ng², Long Teng ³ & Steven Wang ¹ ⊠

Crops require water and fertilizers to grow. However, the shortage of freshwater limits the regions where plants, especially crops, can be grown, and the misuse of chemical fertilizers imposes a burden on the environment and human health. This study develops a self-sufficient system that can passively capture water and produce plant nutrients from the air through the integration of a fog-to-water converter and a spark-type droplet-based electric generator. The proof-of-concept system, based on large-scale 3D wedged spines, achieves a fog-to-water conversion efficiency of 35% and yields nitrogen fertilizer at a rate of 2.38 mg per hour per liter of water droplets. Scaling this system could boost global wheat production by approximately 1 megaton annually, even if operated for a short period each day. This approach offers a self-reliant and potentially eco-friendly solution for agriculture.

Human beings rely on nature to provide the essential resources for survival: food and water. Growing population, overconsumption, and climate change are depleting global water sources and jeopardizing food security. Although the agricultural advancements in the 20th century boosted crop yields and mitigated food shortages, the misuse of chemical fertilizers has taken a toll on the environment and human health¹. Also, water shortages have put 2 billion people worldwide in dire straits and greatly limited the region where crops can be grown, directly or indirectly leading to 690 million people still suffering from malnutrition^{2,3}.

In this work, we developed a system that directly captures water from foggy air and produces nutrients needed for crop growth. The water capture and nutrient production system (WCNPS) comprises a fog-to-water converter (FWC) and a spark-type droplet-based electric generator (SDEG), arranged in a vertical series configuration (Fig. 1a). The device provides water and nitrogenous nutrients for plant germination and growth (Fig. 1c and Supplementary Video 1). The FWC adopts a modular design that consists of multiple fog

harvesting units, as shown in Fig. 1b. Each unit combines the spiky cylindrical hollow structure and the biphilic surface (hydrophilic spots on hydrophobic substrate) (Fig. 1d), allowing a quick droplet detaching rate and improving water collection efficiency to about 35%. This work achieves the largest laboratory-scale FWC with meter-level geometric dimension through modular assembly. Considering both efficiency and scale, the fog harvesting capability of our FWC is an order of magnitude higher than other state-of-the-art works (Fig. 1e and Supplementary Table 1)4-9. The SDEG can convert water droplets from FWC into a high voltage of 6 kV sufficient to generate electric spark (Fig. 1f). The electric sparks that ionize the air every 3 s can yield nitrogen-based fertilizers at an average rate of 2.38 mg/L/h. As a result, our WCNPS can provide water and nutrients for crop growth without any additional energy input and pollutant emissions. It greatly contributes to the growth of crops represented by peas and improves their nutritional value as compared to the blank group, with stem fresh weight, calcium and chlorophyll increased by 22.5%, 3.5% and 141.9%, respectively (Fig. 1g).

¹Department of Mechanical Engineering, City University of Hong Kong, Hong Kong, China. ²School of Energy and Environment, City University of Hong Kong, Hong Kong, China. ³Department of Engineering, University of Cambridge, Cambridge, UK. ⁴These authors contributed equally: Zhenwen Zhang, Tong Li, Yongjiu Yuan, Zhi Zhang. ⊠e-mail: tl322@cam.ac.uk; steven.wang@cityu.edu.hk

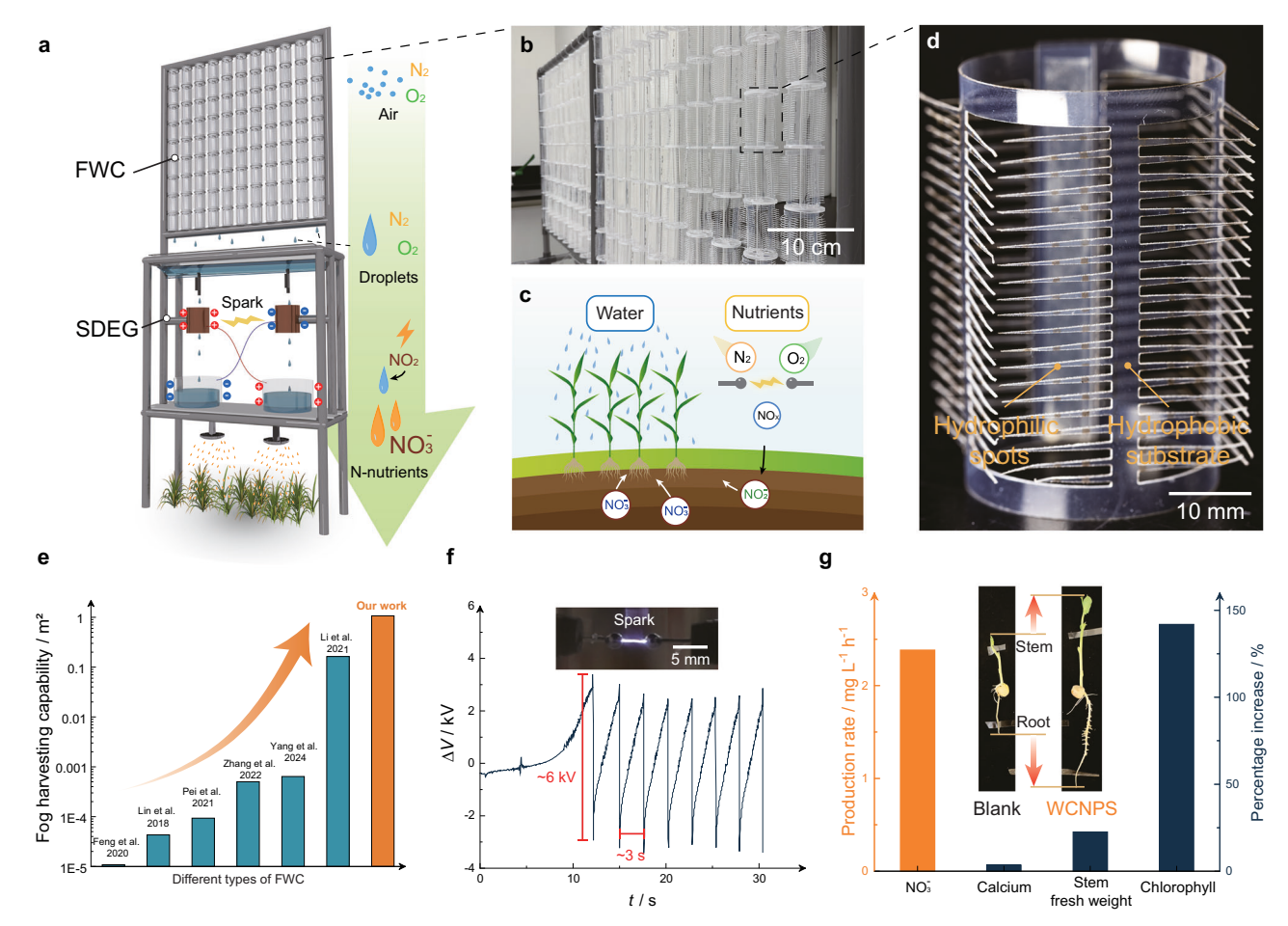


Fig. 1 | **The water capture and nutrient production system (WCNPS). a** Schematic illustration of the structure and working process of WCNPS. The fog-to-water converter (FWC) and the spark-type droplet-based electric generator (SDEG) are arranged in a vertical series configuration. **b** Two sets of fog harvesters placed side by side, which are made up of a number of fog harvesting units and support structures. **c** WCNPS can supply water and nutrients for plant growth. **d** Fog harvesting unit is a spiky cylindrical hollow structure with biphilic surface (hydrophilic spots covering the hydrophobic substrate). **e** Comparison of fog

harvesting capability (FHC) with other studies^{4–9}. $FHC = \eta_{FWC} \times A$, where $\eta_{FWC} = \nu_{co}/\nu_{de}, \nu_{co}$ and ν_{de} are the water collection rate and the water delivery rate, respectively. A is the area of the FWC perpendicular to the fog direction. FHC indicates the application capability of FWC to harvest fog, which is an indicator of comprehensive scale and efficiency. \mathbf{f} The voltage difference (ΔV) during spark generation varies over time (t). \mathbf{g} The positive effects of WCNPS on nitrate production and improving pea growth and nutrients. Source data are provided as a Source Data file.

Results and discussion

The water collection rate is the key to evaluating the performance of FWC. Fog harvesting technology has emerged as a promising solution to mitigate water scarcity, especially in arid and semi-arid areas¹⁰. The effectiveness of the fog harvesting process relies not only on efficient fog interception and condensation but also on rapid and stable droplet transportation. Despite numerous fog harvesting structures that have been developed, including mesh configurations¹¹, harp-shaped arrangements^{12,13}, as well as nature-inspired structures such as spider web-like structures^{14,15}, cactus-like structures^{6,16}, and beetle-like structures^{17,18}, it remains a challenge to achieve both high efficiency and large-scale application. To this end, we integrated the 3D hollow cylinders of cacti and hydrophilic and hydrophobic patterns on the back of beetles into FWCs for the first time, making them scalable and batchable, suitable for large-scale applications (Fig. 2a). The individual units in FWC were fabricated using laser cutting and curled into a three-dimensional (3D) spiky cylindrical hollow structure (Fig. 2b and Supplementary Fig. 1).

In terms of aerodynamics, the cylindrical structure of 3D FWC unit allows fog interception at omnidirectional fog flow, strikingly contrasting with the unidirectional fog flow required by raw 2D FWC (Fig. 2b and Supplementary Fig. 2). Besides, intercepting common fog droplets efficiently is challenging due to their small size, ranging from 200 to 1250 nm¹⁹, and the fact that their Stokes number (0.61–3.81)

indicates that inertial force is not dominant. The Stokes number is given by $St = \rho_w d_w u_{air}/18\mu_{air}$, where d_w is the diameter of the fog droplets, u_{air} is the velocity of air (here is 1 m/s) and μ_{air} is the dynamic viscosity of air. Because of this, most droplets are carried by the airflow and bypass the FWC unless vortices are generated, which can trap scattered small droplets in the vortex to form large droplets that can escape. The diameter of the droplet at the time of escape from the vortex, termed the critical escaping droplet diameter (d_{cri}) , is determined by the air drag force (F_D) and centrifugal force (F_C) . According to the "Burgers vortex"20 and droplet movement inside the vortex theory⁷, $F_D = 3\pi d_d \mu_{air} u_r$, where d_d is the diameter of droplet, μ_{air} is the dynamic viscosity of air and u_r is the velocity of the droplet relative to the fluid, and $F_C = d_d^3 \rho_{water} \Gamma_o^2 r_v / 36\pi \delta^4$, where δ and Γ_o are the size and circulation vortex respectively and r_{ν} is the radial position. The relationship between them determines the motion of a droplet in a vortex. Hence d_{cri} can be expressed as:

$$d_{cri} = \frac{12\pi\mu_{air}\delta}{\Gamma_o\sqrt{\frac{\rho_{air}\rho_{water}}{2}}} \tag{1}$$

Our fog harvesting unit is a 3D geometric structure in which the hollow portion allows the wind to flow through creating more internal

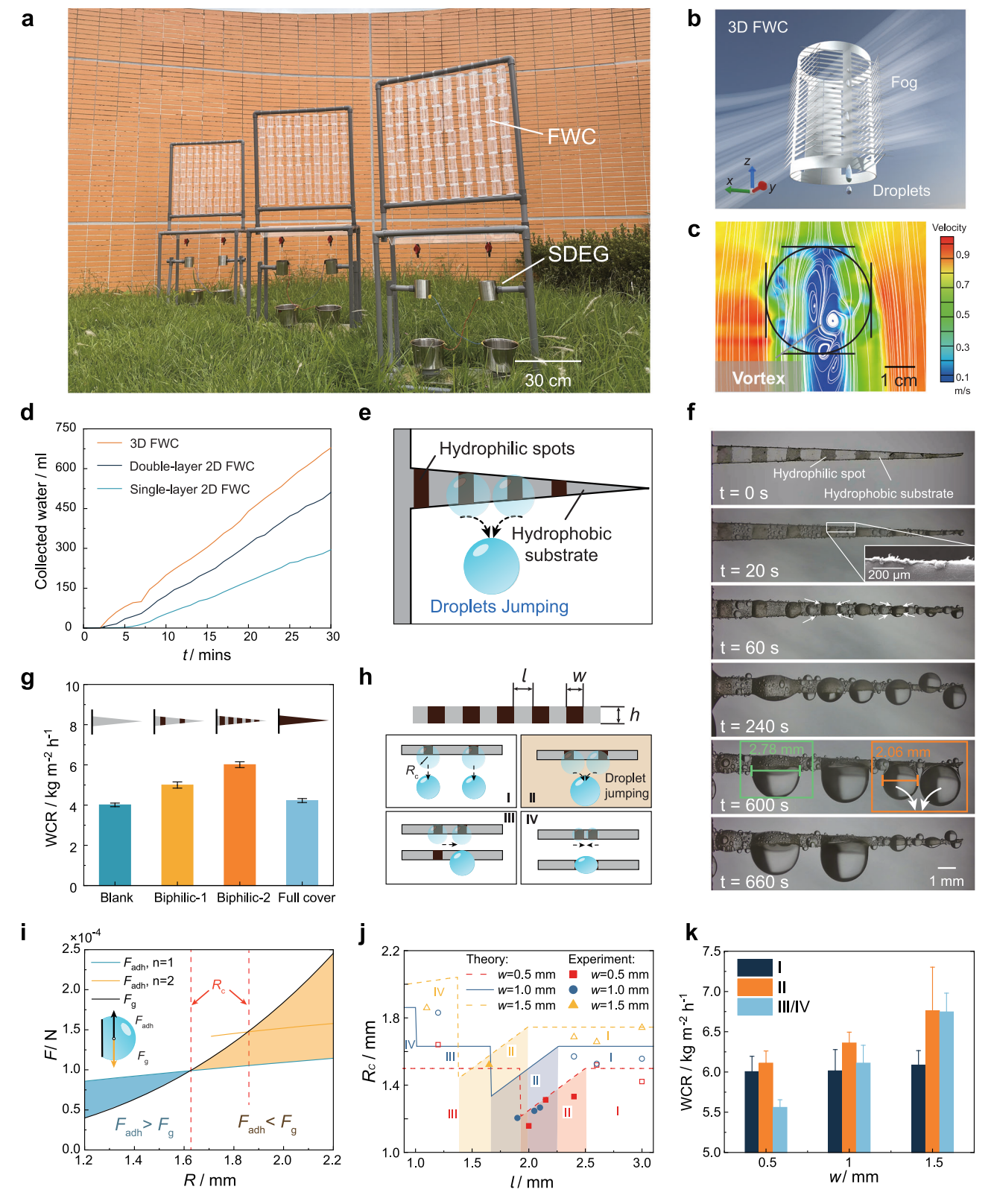


Fig. 2 | **Fog-to-water converter (FWC). a** Three sets of WCNPS, each including the FWC of 0.6×0.6 m². **b** Schematic diagram of 3D FWC subjected to vertical (y direction) fog flow. **c** The particle image velocimetry characterization for 3D FWC units encountering wind from y direction. **d** Collected water of 3D FWC, single-layer and double-layer 2D FWCs with the size of 0.6×0.6 m² (wind speed: -1 m/s, fog flow rate: -5 L/h). **e** Schematic of the biphilic wedged spines surface. **f**, The growth of droplet on the vertical biphilic surface. **g** The water collection rate (WCR) of blank (hydrophobic substrate), biphilic-1(The width of hydrophilic spot is 0.5 mm with a spacing of 3 mm), biphilic-2 (The width of hydrophilic spot is

0.5 mm with a spacing of 2 mm) and full-cover hydrophilic surface. **h** The four layouts of biphilic surfaces classified based on droplet detachment behavior. *l, w* and *h* are spacing, width and height of hydrophilic points. **i** The gravity $\left(F_g\right)$ and adhesion $\left(F_{adh}\right)$ of a droplet on the vertical biphilic surface. *R* is the droplet radius. **j** The critical detachment radius $\left(R_c\right)$ on the vertical biphilic surface with different spacing between hydrophilic spots $\left(l\right)$. **k** The comparison of WCR between fog harvesting units with layout II and other layouts. All error bars indicate \pm SD. Source data are provided as a Source Data file.

vortices (Fig. 2c and Supplementary Fig. 2). The d_{cri} of our 3D FWC is 6.75 μ m according to δ and Γ_o from the particle image velocimetry (PIV) measurement. Therefore, the fog droplets $(d_d < d_{cri})$ are carried into the vortex center by the air and gradually merge into large droplets. When $F_C > F_D$, the large droplet can escape and deposit on solid surfaces. This vortex enhancement effect hardly occurs in a singlelayer 2D FWC (Fig. 2c and Supplementary Video 2) or double-layer 2D FWC (Supplementary Fig. 2) due to the limited vortices. Besides, it is determined that the d_{cri} of double-layers 2D FWC is 36% higher than our 3D FWC, necessitating a longer fog droplet merging time in 2D FWC. These observations highlight the superiority of 3D FWC design over conventional 2D configurations. Furthermore, our fog harvesting units can be assembled into large-scale applications. By stacking units to build a fog harvesting array of 0.36 m² (Fig. 2a), we achieve a water collection rate of approximately 0.67 L every 30 min (Fig. 2d), representing a significant water collection improvement compared with single-layer and double-layer 2D FWCs.

Another distinct feature of our FWC is the biphilic surface (Fig. 2e and Supplementary Fig. 3), inspired by the back of beetles in nature 18,21. We applied a mask method to create an alternately arranged hydrophilic polydopamine coating on the hydrophobic fluorinated ethylene propylene surface (Supplementary Fig. 1). When fog flows around the biphilic spiky surface (Fig. 2f), it deposits on wedged spine surface rapidly in the first few seconds and then merges into many small water droplets at the rough edges (~1 µm in size) cut by the laser, with a noticeably faster rate on the hydrophilic regions. Subsequently, the water droplets on hydrophilic spots absorb small droplets from adjacent regions, leading to rapid size growth. After 600 s, two droplets in the orange rectangle merge together and then rapidly jump off the surface due to the suddenly increased weight (Supplementary Video 3). Notably, the detachment of the jumping droplet occurs earlier compared to droplets that merge prematurely (green rectangle), which reduces the critical detachment droplet diameter by approximately 25.9%, as illustrated in Fig. 2f. Furthermore, it facilitates the exposure of the solid surface, creating more available condensation sites for subsequent fog flows. Hence, the FWC with biphilic surface can obtain a higher water collection rate compared with completely hydrophobic or hydrophilic surfaces, as shown in Fig. 2g. Meanwhile, the different water collection rates of biphilic-1 (the spacing is 3 mm) and biphilic-2 (the spacing is 2 mm) indicate that hydrophilic spot spacing had a significant effect on water collection.

Therefore, we established a theoretical model that examines the interplay between the gravitational force (F_g) and adhesion force (F_{adh}) of droplets to optimize the layout and investigate the mechanism underlying droplet merging and detachment behaviors. The wedged spine is simplified as a rectangle, considering the proximity between two adjacent droplets, as shown in Fig. 2h. Firstly, F_g is determined by the volume of droplets. The droplets adhered to the rectangular spine are shaped as spheres without spherical cap (Fig. 2i), by which we could obtain F_g . Secondly, F_{adh} , that is the vertical component of the surface tension, is obtained by considering the polygonal contact line formed between the droplet and the solid interface²². The specific theoretical model is shown in Methods, Supplementary Fig. 4 and Supplementary Table 2, 3. The gravitational force and adhesion force are expressed as:

$$F_g = k_v \rho_{water} g V_{droplet} \tag{2}$$

$$F_{adh} = \begin{cases} k'_{adh} \left[nw \cos\left(\theta_R^l\right) + (n-1)l \cos\left(\theta_R^b\right) - l_b \cos\left(\theta_A^b\right) \right], \ h < r \le \frac{l_2}{2} \\ k''_{adh} \left[nw \cos\left(\theta_R^l\right) + (n-1)l \cos\left(\theta_R^b\right) + 2l_h \cos\left(\theta_R^b\right) \cos(\alpha) - l_b \cos\left(\theta_A^b\right) \right], \ r > \frac{l_2}{2} \end{cases}$$
(3)

where k_v is the shape correction factor, here taken as 1.2 which is corrected by the experimental data (Supplementary Fig. 4c). ρ_{water} is

the density of water. $V_{droplet}$ is the equivalent volume of the droplet on the vertical spine. k'_{adh} and k''_{adh} are the correction factors, here taken as 0.35 and 0.60, respectively. γ is the surface tension of water. n is the number of hydrophilic spots contained in water droplets. l, w and h are spacing, width and height of hydrophilic points as shown in the Fig. 2h. l_t , l_b and l_h are the lengths of the top, bottom, and hypotenuse of the quadrilateral formed by the droplet in contact with the solid surface. θ^l_R θ^b_R and θ^l_A is the receding contact angle of the hydrophobic surface, the receding and advancing contact angle of the hydrophobic surface.

Based on the above analysis, we can obtain the critical detachment radius (R_c) that represents the radius of the droplet (before merging) when its $F_g = F_{adh}$. It is obvious that when a droplet is adhered to by two hydrophilic points, R_c increase significantly (Fig. 2i), so it is important to try to avoid such a situation. Moreover, four representative layouts are used to summarize the growth and detachment behaviors of droplets on the vertical spiny biphilic surface (Fig. 2h and Supplementary Video 4). Layout I: The spacing between hydrophilic spots is comparatively large enough that a droplet can grow on a single hydrophilic region until it reaches the critical size for detachment. Lavout II: The spacing is decreased to ensure that the adjacent droplets come into contact and merge during the growth process and then jump off because the gravity of the merged droplet exceeds the adhesion force to the solid surface. Layout III: A droplet transfers to another droplet due to the close proximity, and then continues to grow until detachment. Layout IV: The spacing between hydrophilic spots is so close that the merging droplets are adhered by two hydrophilic spots. The most notable is that layout II (highlighted by colored areas) can minimize R_c for different w (Fig. 2j). The experimental results also indicate that R_c of layout II is smaller than that of other layouts. Taking w=0.5 mm as an example, R_c can be reduced by 9.5%–21.8% compared to that on layout I when 1.9 < l < 2.5mm (layout II). We fabricated fog harvesting units with different w based on the theoretical layouts, and the structures with layout II exhibited superior water collection rate compared with that in other layouts (Fig. 2k), up to 6.8 kg/m²/h. Under the same experimental conditions, our 3D FWC is 2.3 times that of the traditional mesh structure and 16% higher than that of the inclined-spikes 3D FWC (Supplementary Fig. 5, 6). The fog collection efficiency has reached more than 35%, and it has excellent wind resistance (Supplementary Fig. 7) and long-term durability (Supplementary Fig. 8, 9).

Given the inherent output characteristics of high voltage and low current, a tailor-made electrostatic generator inspired by Kevin water dropper was designed as the SDEG, which utilizes falling droplets from FWC to generate electric sparks through the electrostatic induction between interconnected systems with opposite charges (Fig. 3a). We must stress that this is the first time to manipulate the spark from the electrostatic generator to produce nutrients from the air. The electric spark is induced by air breakdown, which can efficiently ionize the air and ultimately generate nitrogen-based nutrients required for crop growth. After simplifying SDEG into an equivalent circuit containing capacitors and resistors (Supplementary Fig. 10a)^{23,24}, it can be found that the relationship between voltage difference (ΔV) and time shows an exponential growth trend as:

$$\Delta V(t) = |V_L - V_R| = 2V_0 \exp\left\{ \left[\frac{-(2/R_{RL}) - (1/R) + n_d C_i}{C + 2C_{RL}} \right] t \right\}$$
 (4)

where V_L and V_R are the voltage of left and right metal rings. V_0 is a constant determined by the initial state. R_{RL} and C_{RL} are the resistance and capacitance between the two metal rings, respectively. R is the resistance between the metal ring and surrounding environment. C stands for the capacitance of the equipotential metal ring and container as charge storers. C_i is a capacitance between droplets before detachment and metal rings, a positive value. n_d is the number of falling droplets per second, which is proportional to the water flow rate.

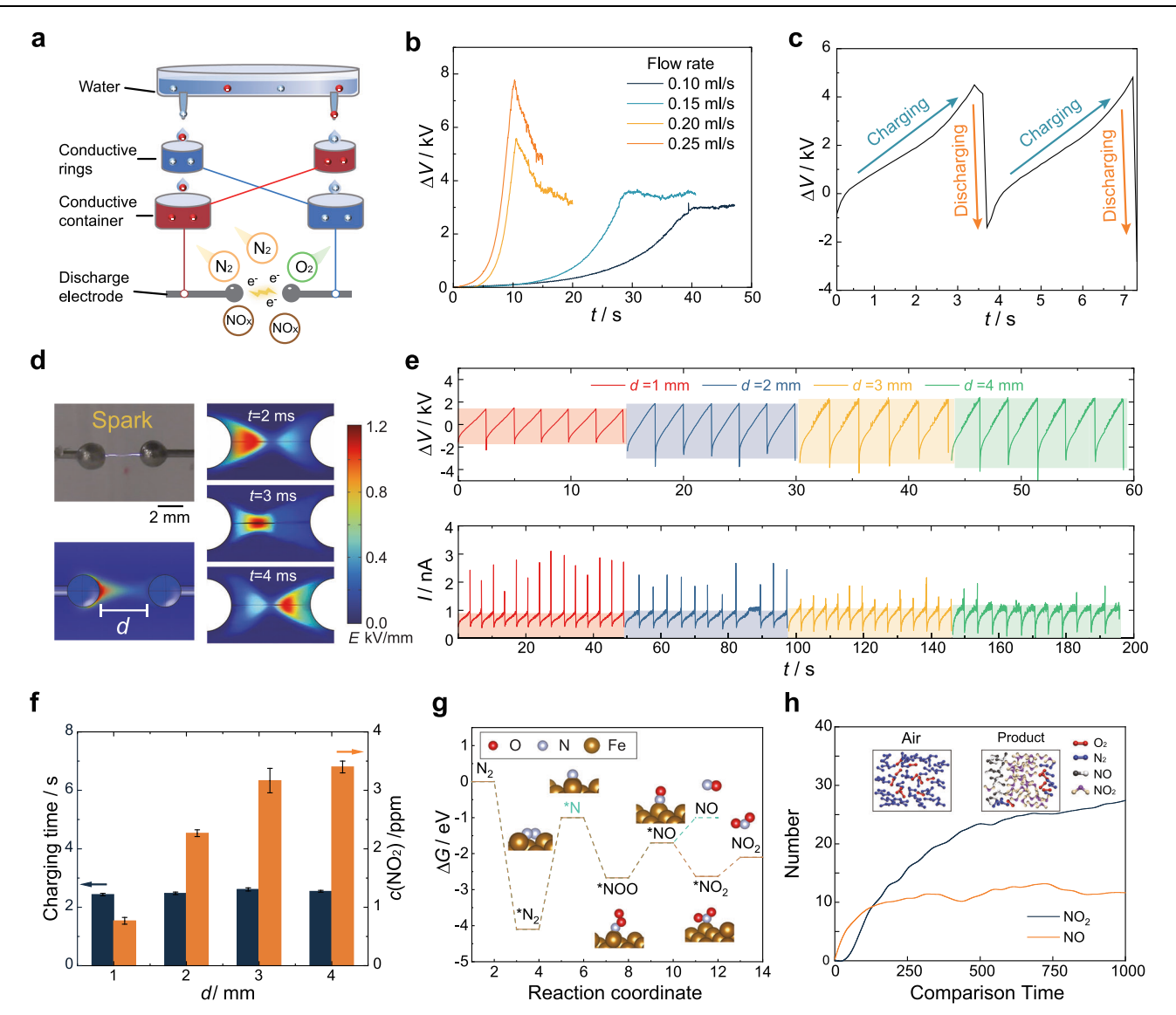


Fig. 3 | **Self-sufficient spark nitrogen fixation. a** Schematic illustration of SDEG achieving electricity generation and electric nitrogen fixation. **b** The voltage difference (ΔV) of the SDEG with time (t) at different water flow rates. **c** The charging and discharging behavior of SDEG. **d** The dynamic variation of electric field intensity (E) during the spark process simulated using COMSOL Multiphysics software. **e** The voltage difference (ΔV) and current (I) under different electrode distances (I). **f** The charging time of one cycle of SDEG (blue bar) and concentration

of nitrogen dioxide $c(NO_2)$ produced of different d after 1 h (orange bar). The volume of the electric nitrogen fixation reactor is 25 mL. ${\bf g}$ The chemical path of the mechanism reactions generating nitric oxide (NO) and NO_2 from air during the spark. ΔG is the Gibbs free energy. ${\bf h}$ The molecular dynamics simulation results of nitrogen fixation using SDEG. All error bars indicate \pm SD. Source data are provided as a Source Data file.

Obviously, n_d positively contributes to the exponential growth rate of $\Delta V(t)$, that indicates the faster the droplets flow through the conductive ring, the faster ΔV rises. Fig. 3b shows the ΔV is proportional to the water flow rate given by the FWC. When the water flow rate is 0.25 mL/s, the voltage difference can quickly rise to 8 kV, and the change over time is according to the exponential function: $\Delta V = 0.068 \exp(0.47t) [kV]$ (Supplementary Fig. 10b). Therefore, this feature contributes to the fact that SDEG can be charged to the breakdown voltage in a short time of ~3 s (Fig. 3c). However, it is worth noting that high humidity environment can cause a significant drop in ΔV and charging speed (Supplementary Fig. 10d). Then comes the discharge stage, where the charge is released rapidly and violently from the electrodes into the air, generating sparks that balance ΔV of the system. The dynamical simulation (Fig. 3d) shows the variation in electric field intensity during the dynamic process from the initiation of spark at one end to the continuation of energy transfer. The local electric field strength can reach 1.2 kV/mm, thereby providing a reliable source basis for subsequent energy conversion. The discharge process is related to the shape of the electrode. Compared with stick and needle-shaped electrodes, spherical electrodes can better save charge and achieve higher breakdown voltage (Supplementary Fig. 10c). Depending on the voltage of the SDEG and the insulation level of air at $3 \, \text{kV/mm}^{25}$, the distance between the electrodes usually needs to be several millimeters. Both the breakdown voltage and current increase as the spherical electrode spacing d (Fig. 3e), thereby increasing the synthesis of NO₂ (Fig. 3f). Although the NO₂ concentration increased by 343.8% from d=1 to 4 mm, the charging time only increased by 0.11 s (4.61%) due to the exponentially increasing voltage (Eq. 4). Hence, it is preferable to maximize the electrode distance while ensuring the ability to discharge accordingly in practical applications.

Unlike the electrochemical and plasma nitrogen fixation that requires high energy consumption and complex supporting equipment, our WCNPS does not require additional energy supply, and the

detailed technical comparisons are listed in Supplementary Table 4. Its nitrogen fixation mechanism is to release a large number of free electrons through the high-voltage discharge of SDEG. These electrons collide with nitrogen and oxygen molecules in the air and decompose into metastable substances such as N and O, and finally generate NO and NO_2 (Eqs. (5)-(8))^{26,27}. We summarized the optimal reaction path of N₂/O₂-to-NO/NO₂ conversion and the optimized geometries are illustrated in Fig. 3g. Gibbs free energy (ΔG) landscapes show the conversion of the *N to *NOO to *NO and *NO₂. Moreover, the conversion of *NOO to *NO₂ displays a lower ΔG when compared to the ΔG of *NOO to *NO, indicating that during the transformation of nitrogen, *NOO transitions through *NO and subsequently spontaneously forms *NO₂. This process ultimately makes the generation of NO₂ easier than that of NO, and the stronger adsorption of NO on the surface of the substrate surface than NO₂ can also explain this (Supplementary Fig. 11). Therefore, in the nitrogen fixation process via spark, the final concentration of NO2 is higher than that of NO. Next, we utilized molecular dynamics to simulate the nitrogen fixation process during spark. Fig. 3h shows the content of relevant gases in the original air and after nitrogen fixation. During the spark, oxygen and nitrogen undergo transformation into NO and nitrogen dioxide NO2 due to instantaneous high temperatures and intense ionization reactions. The changes in the concentrations of NO and NO₂ throughout the spark process demonstrate that during the ongoing nitrogen fixation reactions, the final concentration of NO2 significantly exceeds that of NO.

$$O_{2(g)} + e^- \to 2O_{(v)} + e^-$$
 (5)

$$N_{2(g)} + e^- \rightarrow 2N_{(v)} + e^-$$
 (6)

$$N_{(v)} + O_{(v)} \to NO_{(v)}$$
 (7)

$$NO_{(v)} + O_{(v)} \to NO_{2(v)}$$
 (8)

In the gaseous state, the average production rate of NO_2 produced by the 25 mL spark nitrogen fixation reactor is 1.3 ppm/h (Supplementary Fig. 12a, b). To cultivate plants, the nitrogen oxides produced need to be dissolved in water to form a culture solution. After dissolved in the DI water, a culture solution rich in nitrate (NO^3) and nitrite (NO^2) ions will be formed. According to the results of the ion chromatography tests, the concentration of NO^3 ions increased gradually with the reaction time and could reach -30 mg/L after 10 h, while the concentration of NO^2 ions stayed at a relatively low level of <1 mg/L after 10 h (Fig. 4a). Even when WCNPS was run for 40 h, it could produce about of culture solution containing 100 mg/L NO^3 (Supplementary Fig. 12c).

As a proof of concept, pea was chosen to evaluate the practicality of the nitrogen fertilizer-based nutrient solution obtained directly from the air by the WCNPS due to its fast growth rate. It is evident that compared to the control group using deionized water as the culture medium, the growth of peas was significantly enhanced (Fig. 4b and Supplementary Fig. 12d). The stem height increased by 10.11%, and the root length increased by 90.42% (Fig. 4c). It was visible to the naked eye that the root system of peas cultivated with WCNPS was thicker and had more branches, which was beneficial for the plant's resistance to wind and drought. This method can also improve nitrogen nutrition and plant growth when the base solution is fog water (Supplementary Fig. 13, 14). The growth of wheat, water spinach and daikon under WCNPS cultivation also showed the same promotion (Supplementary Fig. 15). Besides that, the nutritional content of peas cultivated by WCNPS is enhanced, meeting the needs of living organisms more efficiently. The crude protein, vitamin E, vitamin C, calcium and chlorophyll increased significantly (Fig. 4d).

It cannot be ignored that our WCNPS can also adopt electric field enhancement mode for promoting seed germination (Supplementary Fig. 16a), which is crucial for crop yields. Our WCNPS can provide an electric field of up to 60 kV/m to the seeds by connecting the WCNPS to two parallel conductive plates (Supplementary Fig. 16b, c). Pea seeds with an electric field achieve nearly 88% germination rate after half a day, which is significantly better than that of the blank group without electric field stimulation (Fig. 4e and Supplementary Fig. 16d, e). This was effective not only for peas but also for wheat seeds, which had germinated nearly a day earlier (Supplementary Fig. 16f).

Overall, WCNPS is a self-sufficient system that can realize multiple complex processes from fog harvesting to electricity generation to nutrient fixation. From the perspective of the energy conversion process (Fig. 4f), the fog-to-water conversion achieves an efficiency of 35%, and the water droplets overcome the electromagnetic induction force to do work, realizing the conversion of gravitational potential energy to electrical energy. Next, the high-pressure breakdown of the air achieved by the water droplets alone achieves a 25% conversion of electrical energy to chemical energy. Given its excellent performance, we comprehensively evaluated the nutrient harvesting potential of WCNPS applications in four regions that are arid but foggy due to ocean currents. Deploying a 1-km WCNPS every 1 m along the coastline of these areas and operating for 3 h per day could provide up to 11,239 kilotons of water and 99.8 kg of nitrate to the arid areas (Fig. 4g and Supplementary Table 5). WCNPS could achieve a cost of ~0.0049 \$/kg water to produce fresh water (Supplementary Fig. 17 and Supplementary Table 6). These water and fertilizers were expected to increase global wheat production by approximately 1407 kilotons per year, as calculated in "Methods". The WCNPS effectively utilizes the coupled conversion of mechanical, electrical, and chemical energy, operating independently to produce nutrients without additional energy input. This capability is expected to improve the ecological status of arid and barren lands by providing essential nutrients, thereby enhancing agricultural productivity and sustainability.

Methods

Preparation and testing of the fog harvesting units

The thickness of fluorinated ethylene propylene (FEP) film is 0.25 mm. Dopamine hydrochloride, Sodium periodate, sodium acetate and acetic acid were purchased from Macklin. The mask is first cut into a skeletonized shape using laser cutting, and then the mask is adhered to a FEP film and cut with a laser to form a two-dimensional structure with spikes. On the other hand, the process was to synthesize polydopamine. 100 ml of sodium acetate buffer with pH = 5 was first prepared, then 0.2 g of dopamine hydrochloride was added, followed by 0.22 g of sodium periodate and stirred for 5 min²⁸. Next, the cleaned FEP film was put into the solution, left to stand for 2 h, cleaned with deionized water, dried in a vacuum drying oven, and torn off the mask. 2D films were linked head to tail to form a 3D spiky cylindrical hollow structure. In testing the performance of fog harvesting units, the humidifier with a fan was used as a simulated fog source, and the sample was 10 cm away from the fog outlet. The wind speed is 1 m/s, and fog flow rate is 38 mL/h.

The definition of water collection rate and efficiency

The water collection rate is defined as the weight of water collected per unit area of fog-to-water converter per unit time:

$$WCR = \frac{m_{water}}{At} \tag{9}$$

where m_{water} is the weight of the collected water. A is the area of the FWC perpendicular to the fog direction. It is worth noting that this area includes the material-free part of the FWC. t is the running time of FWC.

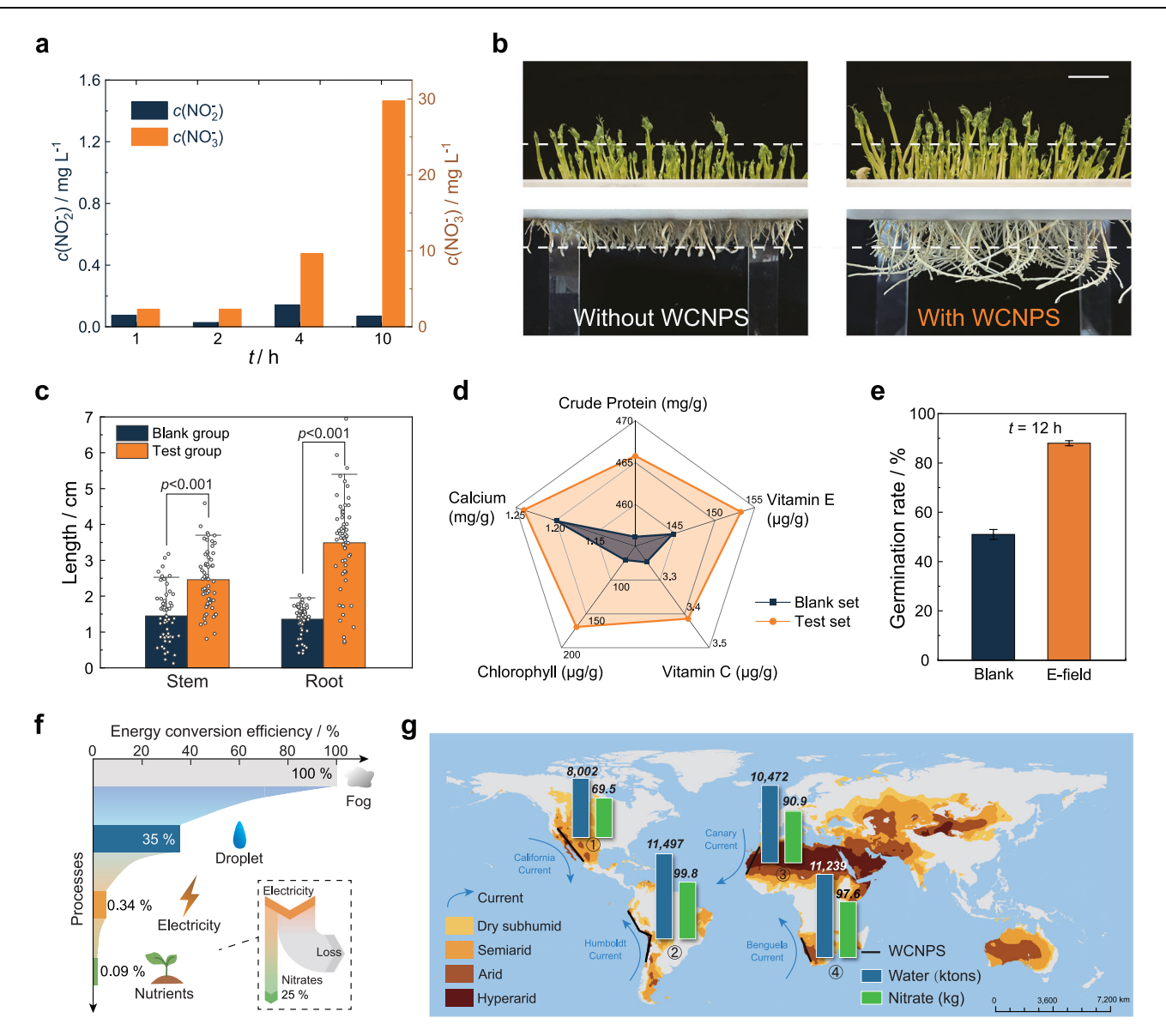


Fig. 4 | **Enhancement of plant germination and growth by WCNPS. a** Concentrations of nitrate $c(NO_3^-)$ and nitrite $c(NO_2^-)$ produced by WCNPS at different times (t) of continuous operation. **b** Stems and roots of peas cultured using the solution produced by WCNPS (test group) vs. that cultured using deionized water (blank group) on the 5th day. Scale bar, 2 cm. **c** Stem and root length

by independent samples t test analysis. **d** Comparison of nutritional content of peas in test and blank groups. **e** Germination rate of pea seeds with and without electric field stimulation for 12 h. **f** Energy conversion efficiency of WCNPS. **g** Potential of water and nitrate that could be produced by WCNPSs constructed along the coastline of arid zones working for 3 h per day (Supplementary Table 5). All error bars indicate \pm SD. Source data are provided as a Source Data file.

The water collection efficiency is defined as the interception rate of fog by the FWC, and the formula is as follows:

statistics of peas in the test and blank groups on the 5th day. P values are evaluated

$$\eta_{FWC} = \frac{\nu_{co}}{\nu_{de}} \tag{10}$$

where ν_{co} and ν_{de} are the water collection rate and the water delivery rate, respectively.

PIV measurement

The pulse laser used in PIV is Vlite-Hi-100 from Beamtech Optronics, the wavelength is 532 nm, the maximum frequency can reach 100 Hz, and the effective working area is over $180 \times 180 \text{ mm}^2$. The CMOS camera used in PIV has a resolution of 2560×1600 , a full-resolution frame rate of 800 Hz, and a minimum inter-frame time interval of 1.4 us. Besides, the inlet cross-section size of the low turbulence wind tunnel is $0.17 \times 0.15 \text{ m}^2$. The turbulence is less than 0.08%.

Modeling the critical detachment radius of water droplets on vertical biphilic surfaces

In the theoretical calculations, assuming that the droplet maintains a fixed contact angle θ on the vertical plane as shown in the Supplementary Fig. 4a, b. Its appearance geometry can be approximated as the remainder of a sphere minus the spherical cap (a portion of a sphere cut off by a plane). The volume and gravity of the droplet change relative to the radius R as in the following equation:

$$V_{droplet} = k_V \frac{\pi}{3} \left[4R^3 - h_{ds}^2 (3R - h_{ds}) \right]$$
 (11)

$$F_g = \rho_{water} V_{droplet} g \tag{12}$$

where k_V is the correction factor, here taken as 1.2, which is corrected by the experimental data (Supplementary Fig. 4c). R is the equivalent radius of a droplet, $R = (R_x + R_y)/2$, R_x and R_y are the radii of the droplet

in the horizontal and vertical directions, respectively. h_{ds} is the distance from the center of the droplet to the solid surface.

The adhesion force on vertical rectangular spines is calculated according to the contact angle of the droplet contact line and the surface tension, which is the combined force of the surface tension in the vertical direction. There are the following assumptions in the theoretical calculations:

- 1. The droplet radius is larger than the width of the spines (*w*), because smaller droplets will not detach and there is no need to calculate the adhesion force.
- 2. The contact angle of a droplet on a solid is fixed and does not change with droplet growth. In addition, the advancing and receding contact angles (θ_A, θ_R) of the droplets on hydrophilic and hydrophobic surfaces, obtained from experimental measurements, are shown in Supplementary Table 2.
- The line of contact between the droplet and solid surface is considered as a straight line.

Accordingly, the adhesion of the vertical rectangular spines to the droplet (F_{adh}) is equal to the combined force of the droplet surface tension acting on the upper and lower contact lines (Eq.(5)). Here it is necessary to classify F_{adh} according to the size of the droplet and the distribution of hydrophilic spots. Firstly, when the diameter of the contact surface of the droplet with solid surface (2r) is less than the distance between the farthest edge of the hydrophilic spots (l_t) , the contact line approximately follows the edge of the hydrophilic spot. Secondly, the contact line forms an approximate isosceles trapezoidal shape, when $r > l_t/2$. In addition, the contact angle of the upper contact line of the droplet is consistent with the surface wettability, as shown in Supplementary Fig. 4d, i.e., the contact angle of the line of contact with the hydrophilic spots is θ_R^l . The contact angle of lower contact line is approximated to be uniformly the advancing angle of the hydrophobic surface (θ_A^b) due to gravity.

$$F_{adh} = \begin{cases} k'_{adh} \left[nw \cos\left(\theta_R^l\right) + (n-1)l \cos\left(\theta_R^b\right) - l_b \cos\left(\theta_A^b\right) \right], \ h < r \le \frac{l_L}{2} \\ k''_{adh} \left[nw \cos\left(\theta_R^l\right) + (n-1)l \cos\left(\theta_R^b\right) + 2l_h \cos\left(\theta_R^b\right) \cos(\alpha) - l_b \cos\left(\theta_A^b\right) \right], \ r > \frac{l_L}{2} \end{cases}$$
(13)

where k'_{adh} and k''_{adh} are the correction factors, here taken as 0.35 and 0.60, respectively. γ is the surface tension of water. n is the number of hydrophilic spots contained in water droplets. l, w and h are spacing, width and height of hydrophilic points as shown in the Fig. 2h. l_t , l_b and l_h are the lengths of the top, bottom, and hypotenuse of the quadrilateral formed by the droplet in contact with the solid surface as shown in Supplementary Fig. 4d. θ_R^l θ_R^b and θ_A^l is the receding contact angle of the hydrophilic surface, the receding and advancing contact angle of the hydrophobic surface.

Therefore, we can calculate the adhesion force for droplets of different radii, and its relation to gravity, as shown in Supplementary Fig. 4e. The value where F_g and F_{adh} are equal is the critical value for droplet detachment from the solid surface. The average errors of the results obtained according to the theory compared to the experimental results were 7.2% (n=1) and 3.1% (n=2), respectively as shown in Supplementary Fig. 4f.

Based on the above analysis, we can obtain the critical detachment radius (R_c) that means the radius of the droplet (before merging) when its $F_g = F_{adh}$. We divided the biphilic surface into four layouts according to the droplet merging behavior shown in Fig. 2h. Layout I: the spacing between hydrophilic spots is comparatively large enough that a droplet can grow on a single hydrophilic region until it reaches the critical size for detachment; Layout II: the spacing is decreased to ensure that the adjacent droplets come into contact and merge during the growth process, and then jump off because the gravity of merged droplet exceeds the adhesion force to the solid surface; Layout III: a

droplet transfers to another droplet due to the close proximity, and then continue to growth until detachment; Layout IV, the spacing between hydrophilic spots is so close that the merging droplets is adhered by two hydrophilic spots.

In the following, we need to determine the critical hydrophilic spots spacing of the four layouts. Firstly, when a droplet grows to the maximum size of detachment at a single hydrophilic spot $R_{max}^{n=1}$, the spacing at which two neighboring droplets can be made to just touch and merge is the critical spacing l_I between Layout I and Layout II, which is expressed by $l_I = 2R_{\text{max}}^{n=1} - w$. Secondly, when the gravity of the large droplet after the merging of two small droplets is not enough to overcome the adhesion force, the large droplet will randomly jump to a hydrophilic spot and continue to grow until it is detached. Therefore, the boundary between Layout II and Layout III is the spacing l_{II} when the gravity of the large droplet is equal to the adhesion force. Thirdly, as the spacing continues to decrease and the edges of the merged large droplets touch the neighboring hydrophilic spot, the droplet will attach to the two hydrophilic spots as shown in Supplementary Fig. 4g, and thus this boundary between Layout III and Layout IV can be expressed as $l_{III} = \sqrt{r^2 - (r - h)^2} - w/2$. Therefore, the size of the critical detaching droplets can be calculated according to the different layouts of the droplets, and the specific results are shown in Supplementary Table 3.

Measurement of electrical characteristics of the electrical generator

Measurement of the voltage of SDEG is carried out using the electrostatic meter (ZEJING, JH-TEST) to observe the operation quickly and without interference. In addition, voltages are measured and recorded using the voltage divider method in conjunction with the oscilloscope (R&S®RTE1000). The current is measured using an electrometer (Keithley 6514) connected in series with the circuit.

Mechanism of the spark-type droplet-based electric generator (SDEG)

The layout of SDEG is shown in Supplementary Fig. 18. Two conductive rings A and B and conductive containers C and D are cross-connected by conductive wires. The collected fog water flows out from the water reservoir above, passes through the valve and passes through the conductive rings A and B respectively. Objects in the atmosphere may have a weak electrostatic imbalance. Here we assume that the conductive ring A has a weak positive charge. When the water flows over A, due to electromagnetic induction, the positive charge contained in the water will be repelled upward, so the water falling into container C will tend to contain more negative charges, which will cause B and C to be negatively charged. Similarly, water droplets passing through ring B will carry more positive charges and fall into D, causing the positive charges in A and D to increase further. As the water droplets fall, more and more charges are separated in the system, causing the voltage difference to increase exponentially.

Dynamic simulation of spark generation

To calculate dynamic electric field dispersion, we use COMSOL 3D and 2D frequency domain simulations of the spherical electrodes, and use physical field interfaces such as electric fields, electromagnetic waves, and dielectric electrics to simulate scenarios.

$$\nabla J = -\frac{\partial t}{\partial \rho_c} \tag{14}$$

$$J = \sigma E \tag{15}$$

where J is the conservative current density, ρ_c is the density of charge, σ is conductivity, and E is electric. ∇J represents the divergence of current density, reflecting the outflow or inflow of charge. We set up a fixed local range of electric fields to collect the electric field intensity between electrodes in millisecond order of time variation. Stainless steel electrode is considered to be the perfect conductor within the COMSOL database. There is an initial spark charging behavior of peak current at the upper, and then passed down.

DFT simulation

The Vienna Ab Initio Package (VASP) was employed to perform all the density functional theory (DFT) simulation within the generalized gradient approximation (GGA) using the Perdew, Burke, and Enzerhof (PBE) formulation²⁹⁻³¹. The projected augmented wave (PAW) potentials were applied to describe the ionic cores and take valence electrons into account using a plane wave basis set with a kinetic energy cut off 400 eV^{32,33}. Partial occupancies of the Kohn-Sham orbitals were allowed using the Gaussian smearing method with a width of 0.05 eV. The electronic energy was considered self-consistent when the energy change was smaller than 10⁻⁵ eV. A geometry optimization was considered convergent when the force change was smaller than 0.05 eV/Å. Grimme's DFT-D3 methodology was used to describe the dispersion interactions³⁴. The vacuum spacing perpendicular to the plane of the structure is 15 Å. The Brillouin zone integral utilized the surfaces structures of $2 \times 2 \times 1$ monk horst pack K-point sampling. Finally, the Gibbs reaction free energy was calculated using the equation³⁵,

$$\Delta G = \Delta E_{\rm dft} + \Delta Z P E - T \Delta S \tag{16}$$

where $\Delta E_{\rm dft}$ is the difference in reaction energy between the reactant and product molecules adsorbed on the catalyst surface, calculated by DFT. Δ ZPE and ΔS are the changes in the zero-point energies and entropy due to the reaction, respectively.

In addition, the adsorption energy ΔE_{ads} is defined as³⁶,

$$\Delta E_{\text{ads}} = E_{\text{svs}} - E_{\text{mol}} - E_{\text{sub}} \tag{17}$$

where E_{sys} is the total energy of adsorbed system, E_{mol} is the energy of an isolated molecule, E_{sub} and is the energy of clean metal substrate.

MD simulation

The MD calculations were using the LAMMPS program with reactive force field ReaxFF and its CHON-2019 parameters. The ReaxFF force field is a force field based on the bond order and the ReaxFF force field includes the following energy components:

$$E_{svst} = E_{bond} + E_{over} + E_{under} + E_{lp} + E_{val} + E_{tor} + E_{vdWaals} + E_{coulomb}$$
 (18)

where terms on the right-hand side of the equation represent bond energy, over-coordination energy penalty, under-coordination stability, lone pair energy, valence angle energy, torsion angle energy, van der Waals energy, and Coulomb energy, respectively.

In this study, we constructed an air model consisting of 600 atoms, with $\rm N_2$ and $\rm O_2$ mixed at a 7:3 ratio and randomly distributed within the simulation domain. Periodic boundary conditions were employed throughout the system, with a time step of 0.1 fs, and the simulation was conducted under an NVT ensemble. An electric field of 4 kV was applied along the z-direction using the fix field command. The temperature of the system was uniformly raised from 300 K to 3000 K over a period of 50 ps, and then maintained at 3000 K for an additional 100 ps.

Cultivation of plants

Peas, wheat, water spinach and daikon seeds were soaked in water for at least 12 h prior to germination. They needed to be covered with moist paper for the first 1–2 days of germination, and the production process was carried out in a grid-like pot of water for cultivation. In experiments to verify the effectiveness of nutrients produced by WCNPS, the experimental and blank groups were grown in the same environment except for the different culture solutions. Then the growth height was counted at regular intervals. In the experiment of electric field enhancement, the experimental group was subjected to the electric field enhancement device shown in Supplementary Fig. 16b. Other conditions are the same as the blank group.

Testing of nutrient produced by WCNPS

Concentration of nitrogen dioxide in gases produced by WCNPS using a nitrogen dioxide detector (EDKORS, ADKS-1) with sampling pump. Concentrations of nitrate and nitrite followers in liquid nutrients produced by WCNPS were tested by ion chromatography (IC). The IC instrument model is DIONEX AQUION, and column model is Dionex IonPac AS19, 4×250 mm. The detector is amperometric detector, and the potassium hydroxide concentration is 20 mmol/L. The column oven temperature 30°C, mobile phase flow rate is 1.0 mL/min, and run time is 20 min. The suppression current is 60 mA, and samples are tested directly on the machine.

Testing of nutritional content in plants

Crude protein: The sample, fresh pea sprouts stems, is digested with sulfuric acid under the action of a catalyst, and the nitrogen-containing compounds are converted into ammonium sulfate. Ammonia is distilled by adding alkali to escape, and then absorbed by boric acid and titrated with a standard sulfuric acid solution to measure the nitrogen content. Then calculate the crude protein content as:

$$Crude\ protein(N) = \frac{k_N M_N c (V - V_0)}{m}$$
 (19)

where k_N is average conversion coefficient of nitrogen into crude protein. M_N is molar mass of N, g/mol. c is concentration of acid standard solution, mol/L. V is volume of acid standard solution used to titrate the sample, mL. m is mass of sample, g. Vitamins C: HPLC-MS/MS method (Agilent 1260 LC coupled to Xevo TQ-s mass spectrometer). Vitamins E, chlorophyll and calcium: colorimetry method measured by a spectrophotometer.

Energy conversion efficiency of WCNPS

Firstly, in the process of fog harvesting, we only consider the gravitational potential energy contained in the fog, so the energy conversion efficiency from fog to water droplets is the water collection efficiency of FWC. Secondly, in the process of water droplets turning into electricity, the water droplets overcome electromagnetic induction and do work in the process of falling, thus realizing the conversion of gravitational potential energy. Therefore, the conversion efficiency of water droplets turning into electricity is

$$\eta_{d2e} = \frac{E_e}{E_p} = \frac{mgh}{\int U(t)I(t)dt}$$
 (20)

where E_p is the gravitational potential energy of falling droplets during charging. E_e is the electrical energy generated per discharge, $E_e = \int U(t)I(t)dt$, U(t) and I(t) are the transient voltage and current during the discharge stage. Thirdly, in the process of electric nitrogen fixation, the energy released by electricity stimulates the synthesis of nitrogen dioxide. This energy conversion efficiency from electricity to chemical is:

$$\eta_{e2c} = \frac{E_c}{E_e} \tag{21}$$

where $E_p = M_{NO2}\Delta H$, M_{NO2} is number of moles of NO₂ produced during one discharge, mol. ΔH is reaction heat to generate 1 mol NO₂, here is 67.8 kJ/mol.

Calculation of water and nutrients produced by largescale WCNPS

Here we assume that all wheat fields in the world (230 million hectares) are equipped with WCNPS with a height of 5 m. The front and rear rows of equipment are 1 m apart. The growing cycle of wheat is usually 6 months. Assuming there are 3 h of fog every day, the flow rate of fog is $1300~{\rm g~m^{-2}~h^{-1}}$, and the yield of nitrate is $0.0125~{\rm mg~h^{-1}}$, $1.79\times10^{10}~{\rm kg}$ of water and $1.56\times10^8~{\rm kg}$ of nitrogen fertilizer (nitrate) can be produced during the wheat growth cycle. Wheat typically requires around 2–3 kg of nitrogen (N) per $100~{\rm kg}$ of gain yield. At this case, we use an average value of $2.5~{\rm kg}$ of nitrogen³⁷. Therefore, we can obtain that producing $100~{\rm kg}$ of wheat requires approximately $11.06~{\rm kg}$ of nitrates to provide the required nitrogen. This amount may vary slightly depending on specific agricultural practices and the exact nitrogen requirements of the wheat variety being grown. Combining the above, it can be concluded that the large-scale application of WCNPS can increase global wheat production by $1407~{\rm kilotons}$ per year.

Reporting summary

Further information on research design is available in the Nature Portfolio Reporting Summary linked to this article.

Data availability

All data supporting the findings of this study are available within the article and its supplementary files. Source data are provided with this paper.

References

- Carvalho, F. P. Pesticides, environment, and food safety. Food Energy Security 6, 48-60 (2017).
- 2. WHO. Summary Progress Update 2021: SDG 6 water and sanitation for all (2021).
- 3. FAO, I., UNICEF, WFP and WHO. The State of Food Security and Nutrition in the World 2023. 316 p. (2023).
- Yang, D., Ramu, A. G. & Choi, D. Multifunctional integrated pattern for enhancing fog harvesting water unidirectional transport in a heterogeneous pattern. npj Clean. Water 7, 20 (2024).
- Pei, W. et al. Excellent fog harvesting performance of liquid-infused nano-textured 3D frame. Chem. Eng. J. 409, 128180 (2021).
- Zhang, S. et al. Bioinspired asymmetric amphiphilic surface for triboelectric enhanced efficient water harvesting. *Nat. Commun.* 13, 4168 (2022).
- Li, J. et al. Aerodynamics-assisted, efficient and scalable kirigami fog collectors. Nat. Commun. 12, 5484 (2021).
- 8. Feng, J., Zhong, L. & Guo, Z. Sprayed hieratical biomimetic superhydrophilic-superhydrophobic surface for efficient fog harvesting. *Chem. Eng. J.* **388**, 124283 (2020).
- Lin, J., Tan, X., Shi, T., Tang, Z. & Liao, G. Leaf vein-inspired hierarchical wedge-shaped tracks on flexible substrate for enhanced directional water collection. ACS Appl. Mater. Interfaces 10, 44815–44824 (2018).
- Lekouch, I. et al. Dew, fog, and rain as supplementary sources of water in south-western Morocco. *Energy* 36, 2257–2265 (2011).
- Park, K.-C., Chhatre, S. S., Srinivasan, S., Cohen, R. E. & McKinley, G. H. Optimal design of permeable fiber network structures for fog harvesting. *Langmuir* 29, 13269–13277 (2013).
- Shi, W., Anderson, M. J., Tulkoff, J. B., Kennedy, B. S. & Boreyko, J. B. Fog harvesting with harps. ACS Appl. Mater. Interfaces 10, 11979–11986 (2018).

- Kaindu, J. K. et al. Antitangling and manufacturable Fog Harps for high-efficiency water harvesting. *Droplet* 2, e78 (2023).
- Liu, Y. et al. Bioinspired nanofibril-humped fibers with strong capillary channels for fog capture. ACS Appl. Mater. Interfaces 12, 28876–28884 (2020).
- Tian, Y. et al. Large-scale water collection of bioinspired cavitymicrofibers. Nat. Commun. 8, 1080 (2017).
- Ju, J. et al. A multi-structural and multi-functional integrated fog collection system in cactus. Nat. Commun. 3, 1247 (2012).
- Hou, Y. et al. Tunable water harvesting surfaces consisting of biphilic nanoscale topography. ACS Nano 12, 11022–11030 (2018).
- Parker, A. R. & Lawrence, C. R. Water capture by a desert beetle. Nature 414, 33–34 (2001).
- Hung, D. V. et al. Measurements of particle size distributions produced by humidifiers operating in high humidity storage environments. *Biosyst. Eng.* 107, 54–60 (2010).
- 20. Burgers, J. M. in *Advances in Applied Mechanics* Vol. 1 (eds Richard Von Mises & Theodore Von Kármán) 171-199 (Elsevier, 1948).
- Dai, H., Dong, Z. & Jiang, L. Directional liquid dynamics of interfaces with superwettability. Sci. Adv. 6, eabb5528 https://doi.org/10. 1126/sciadv.abb5528.
- Chini, S. F., Bertola, V. & Amirfazli, A. A methodology to determine the adhesion force of arbitrarily shaped drops with convex contact lines. Colloids Surf. A: Physicochem. Eng. Asp. 436, 425–433 (2013).
- Huang, H.-F. Voltage build-up time responses of Kelvin's water droplet generator: Variations due to different geometric configurations. J. Electrost. 72, 447–456 (2014).
- 24. Zahn, M. Self-excited ac high voltage generation using water droplets. *Am. J. Phys.* **41**, 196–202 (1973).
- Rigden, J. S. Macmillan Encyclopedia of Physics. (Simon & Schuster Macmillan, 1996).
- Wong, M.-C., Xu, W. & Hao, J. Microplasma-discharge-based nitrogen fixation driven by triboelectric nanogenerator toward selfpowered mechano-nitrogenous fertilizer supplier. Adv. Funct. Mater. 29, 1904090 (2019).
- Van Alphen, S. et al. Effusion nozzle for energy-efficient NOx production in a rotating gliding arc plasma reactor. *Chem. Eng. J.* 443, 136529 (2022).
- Ponzio, F. et al. Oxidant control of polydopamine surface chemistry in acids: A mechanism-based entry to superhydrophilicsuperoleophobic coatings. Chem. Mater. 28, 4697–4705 (2016).
- 29. Kresse, G. & Furthmüller, J. Efficient iterative schemes for ab initio total-energy calculations using a plane-wave basis set. *Phys. Rev. B* **54**, 11169–11186 (1996).
- Perdew, J. P., Burke, K. & Ernzerhof, M. Generalized gradient approximation made simple. *Phys. Rev. Lett.* 77, 3865–3868 (1996).
- 31. Kresse, G. & Joubert, D. From ultrasoft pseudopotentials to the projector augmented-wave method. *Phys. Rev. B* **59**, 1758–1775 (1999).
- 32. Blöchl, P. E. Projector augmented-wave method. *Phys. Rev. B* **50**, 17953–17979 (1994).
- Grimme, S., Antony, J., Ehrlich, S. & Krieg, H. A consistent and accurate ab initio parametrization of density functional dispersion correction (DFT-D) for the 94 elements H-Pu. J. Chem. Phys. 132 https://doi.org/10.1063/1.3382344 (2010).
- Henkelman, G., Uberuaga, B. P. & Jónsson, H. A climbing image nudged elastic band method for finding saddle points and minimum energy paths. J. Chem. Phys. 113, 9901–9904 (2000).
- 35. Xu, H., Cheng, D., Cao, D. & Zeng, X. C. Revisiting the universal principle for the rational design of single-atom electrocatalysts. *Nat. Catal.* **7**, 207–218 (2024).
- Gao, W. et al. Determining the adsorption energies of small molecules with the intrinsic properties of adsorbates and substrates. *Nat. Commun.* 11, 1196 (2020).

Warncke, D., Dahl, J., Jacobs, L. & Laboski, C. Nutrient recommendations for field crops in Michigan. (Michigan State University Extension East Lansing, MI, 2009).

Acknowledgements

We acknowledge the financial support from Research Grants Council of Hong Kong. Research Grants Council of Hong Kong (No. 11217523).

Author contributions

Conceptualization: S.W., Z.Z. (Z.W. Zhang), T.L. (T. Long). Methodology: Z.Z. (Z.W. Zhang), T.L. (T. Li), Y.Y., Z.Z. (Z. Zhang), C.L. Investigation: Z.Z. (Z.W. Zhang), T.L. (T. Li), Y.Y., Z.Z. (Z. Zhang), C.L., X.Y., H.W., W.K.L., Q.X., J.L., Y.H.N., T.L. (T. Long), S.W. Visualization: Z.Z. (Z.W. Zhang), T.L. (T. Li), Z.Z. (Z. Zhang), C.L., X.Y. Funding acquisition: S.W. Supervision: S.W. Writing—original draft: S.W., Z.Z. (Z.W. Zhang), T.L. (T. Li), Y.Y., Z.Z. (Z. Zhang). Writing—review & editing: Z.Z. (Z.W. Zhang), T.L. (T. Li), T.L. (T. Long), S.W.

Competing interests

The authors declare no competing interests.

Additional information

Supplementary information The online version contains supplementary material available at https://doi.org/10.1038/s41467-025-60340-0.

Correspondence and requests for materials should be addressed to Long Teng or Steven Wang.

Peer review information *Nature Communications* thanks the anonymous reviewer(s) for their contribution to the peer review of this work. A peer review file is available.

Reprints and permissions information is available at http://www.nature.com/reprints

Publisher's note Springer Nature remains neutral with regard to jurisdictional claims in published maps and institutional affiliations.

Open Access This article is licensed under a Creative Commons Attribution-NonCommercial-NoDerivatives 4.0 International License, which permits any non-commercial use, sharing, distribution and reproduction in any medium or format, as long as you give appropriate credit to the original author(s) and the source, provide a link to the Creative Commons licence, and indicate if you modified the licensed material. You do not have permission under this licence to share adapted material derived from this article or parts of it. The images or other third party material in this article are included in the article's Creative Commons licence, unless indicated otherwise in a credit line to the material. If material is not included in the article's Creative Commons licence and your intended use is not permitted by statutory regulation or exceeds the permitted use, you will need to obtain permission directly from the copyright holder. To view a copy of this licence, visit http://creativecommons.org/licenses/by-nc-nd/4.0/.

© The Author(s) 2025